

Stability of high-fidelity two-qubit operations in silicon

Tuomo Tanttu,^{1, 2, *} Wee Han Lim,^{1, 2} Jonathan Y. Huang,¹ Nard Dumoulin Stuyck,^{1, 2} Will Gilbert,^{1, 2} Rocky Y. Su,¹ MengKe Feng,¹ Jesus D. Cifuentes,¹ Amanda E. Seedhouse,¹ Stefan K. Seritan,³ Corey I. Ostrove,³ Kenneth M. Rudinger,³ Ross C. C. Leon,^{1, †} Wister Huang,^{1, ‡} Christopher C. Escott,^{1, 2} Kohei M. Itoh,⁴ Nikolay V. Abrosimov,⁵ Hans-Joachim Pohl,⁶ Michael L. W. Thewalt,⁷ Fay E. Hudson,^{1, 2} Robin Blume-Kohout,³ Stephen D. Bartlett,⁸ Andrea Morello,¹ Arne Laucht,^{1, 2} Chih Hwan Yang,^{1, 2} Andre Saraiva,^{1, 2} and Andrew S. Dzurak^{1, 2, §}

¹*School of Electrical Engineering and Telecommunications, UNSW, Sydney, NSW 2052, Australia*

²*Diraq, Sydney, NSW, Australia*

³*Quantum Performance Laboratory, Sandia National Laboratories, Albuquerque, NM, USA.*

⁴*School of Fundamental Science and Technology, Keio University, Yokohama, Japan*

⁵*Leibniz-Institut für Kristallzüchtung, 12489 Berlin, Germany*

⁶*VITCON Projectconsult GmbH, 07745 Jena, Germany*

⁷*Department of Physics, Simon Fraser University, British Columbia V5A 1S6, Canada*

⁸*Centre for Engineered Quantum Systems, School of Physics,*

University of Sydney, Sydney, New South Wales 2006, Australia

(Dated: March 8, 2023)

Stable entangling operations between qubits are essential for the efficient performance of multi-qubit systems and will be a crucial factor in avoiding errors in full-scale quantum processors. Recent demonstrations on a number of different silicon spin qubit platforms have indicated promising two-qubit gate fidelities at the threshold required for quantum error correction, with errors below around one percent, however, further understanding of the stability of such fidelities is required to assess the true prospects for fault-tolerant quantum computing. Here we demonstrate the first operation of two-qubit gates with fidelities above 99% in the technologically important silicon metal-oxide-semiconductor (SiMOS) quantum dot platform. We undertake a detailed study of the stability of two-qubit operations in silicon, as required for scalable quantum computing, by analyzing errors and fidelities in multiple devices through numerous trials and Extended periods of operation. Our characterisation methods indicate fidelities ranging from 96.8% to 99.8%, putting these qubits at the threshold required for error correction. Our analysis tools also identify physical causes of qubit degradation and offer ways to maintain performance within tolerance. Furthermore, we investigate the impact of qubit design, feedback systems, and robust gates on implementing scalable, high-fidelity control strategies. These results highlight both the capabilities and challenges for the scaling up of spin-based qubits into full-scale quantum processors.

Building a full-scale quantum computer is one of the great scientific and engineering challenges of our time. Spin qubits based on silicon metal—oxide—semiconductor (SiMOS) quantum dots hold great promise for achieving this goal, thanks to the widespread in-place industrial facilities, long coherence times, and compatibility with pumped He systems[1–6]. Recently, two-qubit (2Q) gate fidelities for spin qubits in SiGe and donors in SiMOS have surpassed the 99% threshold required for the surface code [7–12]. To achieve a scalable SiMOS quantum computer, it is important to focus on scalable operation principles, such as abandoning schemes with always-on couplings [9, 13], minimizing feedback needs [13, 14], and choosing a single high-performing "hero" device. Reducing error correction overheads is key, and can be achieved by maximizing the averaged 2Q gate fidelity while minimizing variability.

Our study uses three different SiMOS devices and operates pulsed interstitial exchange gates with two types of gates: controlled phase (CZ) and decoupled con-

trolled phase (DCZ) gates [15]. Three different protocols for characterising gate errors are used, interleaved randomised benchmarking (IRB) [16, 17], gate set tomography (GST) [18, 19], and fast Bayesian tomography (FBT) [20]. Our IRB results demonstrate an average 2Q gate fidelity of 99.16% (ranging from 98.4% to 99.76% over multiple measurements), while FBT results range from 98.1% to 99.1%. GST experiments on two devices showed fidelities of 96.8% and 98.0%. However, feedback schemes were needed for the two devices, which will be difficult to scale up. One device did not require feedback, demonstrating the potential to reach error tolerance in large arrays without excessive feedback. The system evolves over time due to drifts, in the nuclear and charge environment, which we capture using FBT analysis of long IRB runs. Additionally, we observe that cross-talk and decoherence are limiting the single qubit fidelities in the context of multi-qubit operation [10]. The exact operative thresholds for the error correction depend on the exact biases of the gate and SPAM errors and it is possible to compensate errors in one channel with a good

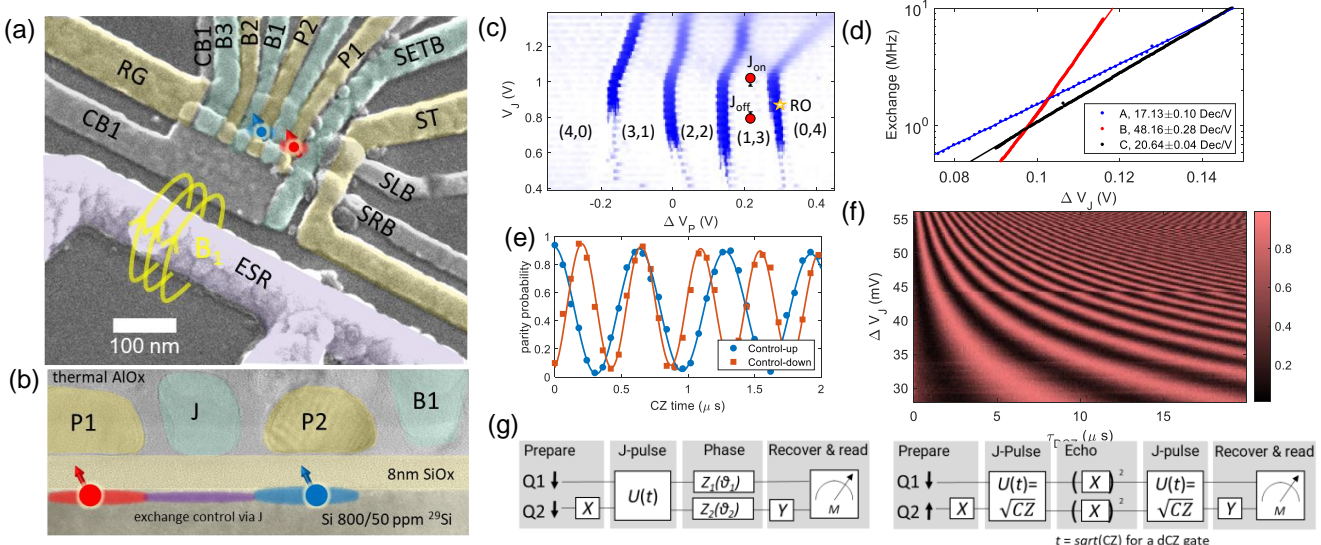


Figure 1 | Electrostatic quantum dots with tunable energy spectrum. **a**, False color scanning electron micrograph (SEM) of the device similar to A and B. **b**, False color transmission electron micrograph (TEM) of a cross section of a device similar to A and B together with the schematic location of the qubit dots. **c**, A stability map in device A used in isolated mode together with the important operation points for qubit operation (J_{on} and J_{off}) and readout (RO). **d**, The experimental turn on rate for devices A, B and C together with exponential fits. **e**, CZ oscillations using the measurement sequence in **g** with two different control qubit initialisations. **f**, Oscillations of DCZ gate sequence as a function of time and voltage level. **g**, Pulse sequences used in the experiments for CZ and DCZ in **e** and **f**.

performance on another [21]. To reach fault-tolerance, we need to be able to achieve at least few hundred gate operations without errors [7].

Although these results show that the error-correcting threshold is achievable in SiMOS, further work is needed to achieve this threshold in larger arrays for all primitive gates. Possible solutions include materials development, refined device designs, operational engineering for noise resilience, and increasing Rabi speed using dielectric resonators or similar microwave engineering [22–25]. We conclude that overcoming these hurdles is within reach of current technology.

RESULTS

An example of similar of the three different devices — A, B, and C — used for our experiments is shown in Fig. 1a. A and B have been used in earlier experiments [26]. To provide magnetically quiet environment to our qubits, we use isotopically purified ^{28}Si with 800 ppm (A and B) or 50 ppm (C) residual ^{29}Si . We control the electron spin qubits accumulated under the plunger gates (P1 and P2) by operating the exchange barrier gate (J) in between. Figure 1b shows a transmission electron micrograph (TEM) of a cross-section of a similar device, along with the schematic of the 2Q operation principle. Note that to avoid variation in the pitch sizes (i.e. controllability) all the plunger gates are done in a single lithographic run and all exchange gates in another one. Figure 1c displays the operative voltage region and charge stability

map and the operation points from device A in isolated mode, while the rate of turn-on of the exchange is shown in Fig. 1d. Stability maps of B and C can be seen in Extended Figs. 1a and c. We use Pauli spin blockade based parity readout for state measurement [27, 28]. In the extended Table I, we show the characteristics of all the devices.

We use five different basic gates that we use to construct the full 2Q Clifford gate space. Gates $X_1^{\pi/2}$, $X_2^{\pi/2}$, $Z_1^{\pi/2}$, $Z_2^{\pi/2}$ are quarter turns around the respective axes for the target qubit. We use two different 2Q gate implementations in our devices. A single square exchange gate pulse implements CZ gate, or two equal length exchange pulses separated by single qubit pulses on both qubits is the implementation of the DCZ gate [15], both gate sequences depicted in Fig. 1g. The decoupling pulses between exchange pulses suppress quasistatic noise of the single qubits, such as noise caused by residual ^{29}Si . The oscillations induced by the turn-on of the exchange for two different initialisations in device A by the CZ pulse sequence is shown in Fig. 1e. Based on the diff. In Fig. 1f we show the DCZ oscillations in device B as a function of total exchange time and level. In device A we benchmark CZ gate and in devices B and C we benchmark DCZ gate

To run long gate error characterisation measurements, we perform feedback on all qubits in devices A and B, such as Larmor and Rabi frequency feedbacks and exchange gate pulse amplitude and phase corrections. As the number of qubits grow in the quantum computer, running such many feedbacks for each qubit and their

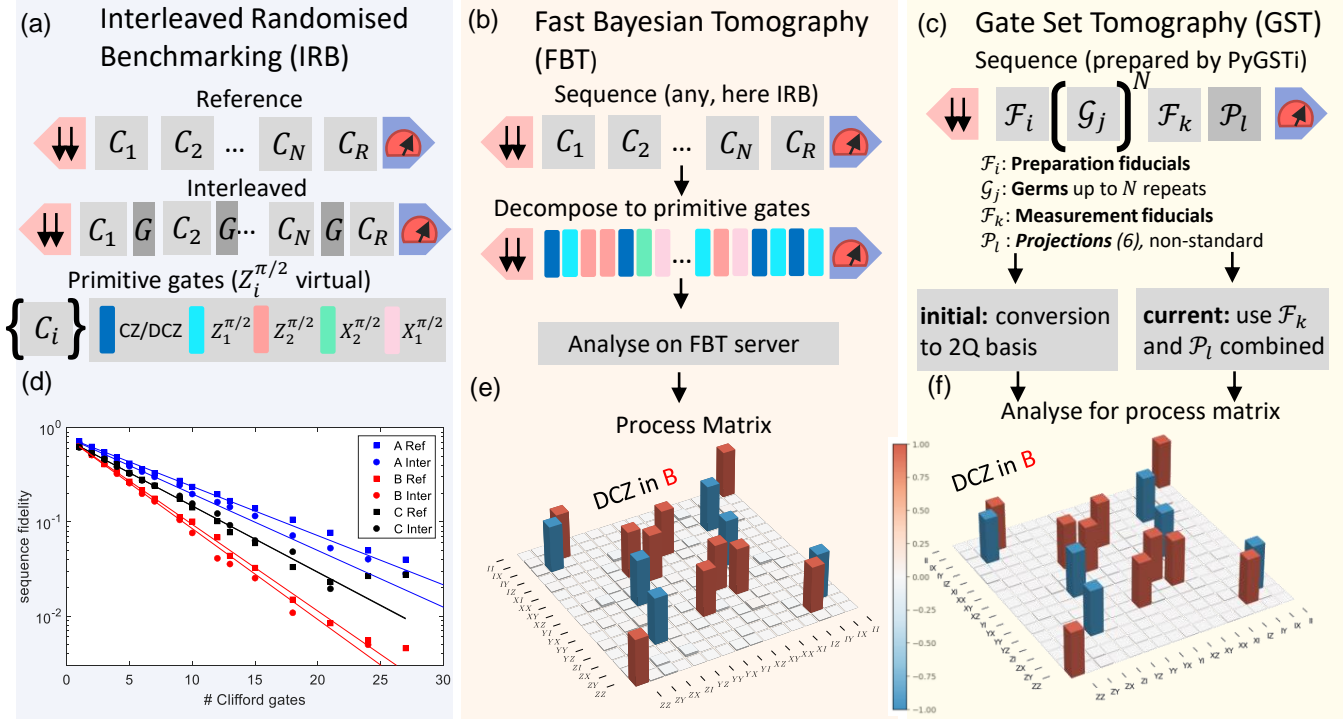


Figure 2 | Results of error characterisation methods **a**, Measurement sequence principle used in randomised benchmarking. In gate of interest is interleaved with a sequence of random Clifford sequences that are composed of in total five primitive gates. **b**, Simplified fast Bayesian tomography workflow from experiment to result. FBT can analyse any gate sequence, IRB used as an example. **c**, Gate set tomography workflow used in our experiment. **d**, Recovery probability of the randomised benchmarking sequence as a function of Clifford gates both for interleaved and reference sequences in all devices. **e**, Process matrix of DCZ operator in device B extracted using FBT analysis on the IRB data. **f**, Process matrix of DCZ operator in device B extracted using GST analysis on GST measurement data.

intermediate gates would significantly increase the overhead of running a large scale quantum computer. In device C we ran the experiment without any qubit feedbacks and still retained a high fidelity, demonstrating a capability of a more scalable feedback.

Gate error characterisation methods

TABLE I. Error characterisation methods in this paper.

Method	Measurement	Analysis	process matrix
IRB	Randomised Cliffords	decay fit	no
FBT	Any gate sequence	Bayesian estimation	yes
GST	Periodic info-complete fiducials	Maximum-likelyhood	yes

In order to assess the performance of the device, three error characterisation methods were employed; IRB, FBT and GST. Table I summarises these methods briefly. The IRB method involves determining the Clifford fidelity by measuring the survival probability of randomized Clifford sequences as a function of sequence length. The interleaved gate fidelity is obtained by dividing the interleaved decay rate by the reference decay rate, with more details explained in the supplementary discussion: Randomised benchmarking. Figure 2a demonstrates this

principle with $X_1^{\pi/2}$, $X_2^{\pi/2}$, $Z_1^{\pi/2}$, $Z_2^{\pi/2}$, and CZ/DCZ gates. Figure 2d shows examples of the interleaved randomised benchmarking and the corresponding reference sequences. The results of multiple IRB runs are summarised in Fig. 3a and Extended Table II, with average interleaved gate fidelities over all IRB measurements of 98.4%, 99.3%, and 99.78% in devices A, B, and C respectively. The information from the individual sequences can be used to obtain the process matrix of the underlying gates using FBT [20].

The FBT method involves decomposing the RB sequences into the primitive gates and feeding the measurement results in the parity basis to the online FBT server for analysis (schematic shown in Fig. 2b). The Bayesian posteriori of the process matrices is updated based on the results. Figure 2e shows an example of a process matrix from the FBT analysis of device B, and Extended Table II lists the fidelities for all devices. The error generators for different gates are shown in the Extended Figure 2.

We perform a novel variation of two-qubit GST [8] adapted to the unique properties of this system (see Fig. 2c). Previous experiments leveraged simultaneous readout of both qubits individually, which is described by a four-outcome positive operator-valued measure (POVM) $\{|00\rangle\langle 00|, |01\rangle\langle 01|, |10\rangle\langle 10|, |11\rangle\langle 11|\}$. Our

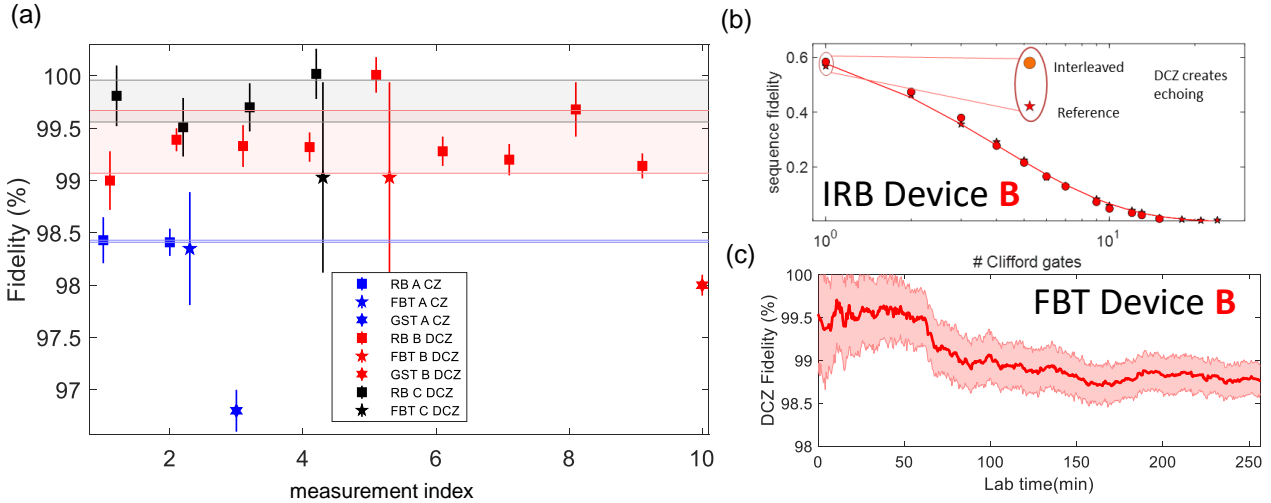


Figure 3 | Fidelities from error characterisation runs. **a**, Two-qubit gate fidelities extracted from different error characterisation measurements of IRB, and GST. The fidelity of the FBT analysis from certain IRB is the neighboring data point. This data is also in the Extended Table II. **b**, DCZ fidelity trace as a function of lab time, where the transient fidelities are extract from FBT analysis on IRB experiment data. **c**, Fidelity trace as function of lab time of device B. Fidelity extracted from IRB experiment by FBT. Error bars of fidelity are estimated by re-sampling the noise channel parameters by Gaussian distribution for 100 times.

systems use a parity readout, described by a two-outcome POVM $\{|00\rangle\langle 00| + |11\rangle\langle 11|, |10\rangle\langle 10| + |01\rangle\langle 01|\}$. This requires only one change to the GST experiment design: definition of a new and slightly larger set of “measurement fiducial” circuits. Measurement fiducials, labeled \mathcal{F}_k in Fig. 2c, are short subcircuits used to probe an informationally complete set of different observables. The measurement fiducial construction used for this experiment is described in the Supplementary Discussion: Gate Set Tomography with parity readout, where we also compare our results to an emulated “standard GST” experiment on this device. The observed outcome frequencies for all GST circuits are fed into the GST analysis software package pyGSTi [29], which returns estimates of the gate process matrices. GST’s estimate of the DCZ gate is shown in Fig. 2f, and in the Extended Tables III(a) and III(b) we quantify the errors in our gates using two metrics, generator infidelity and total error [8, 30]. In these tables we’ve additionally partitioned both metrics according to their support in order to distinguish errors that occur locally on a gate’s target qubit from ones afflicting a spectator qubit (e.g., due to crosstalk, see the Supplementary Discussion: Gate Set Tomography with parity readout for more details).

Gate operation characterisations

There are some important take aways from the Extended table II. One is that the gate fidelity varies from experiment to another even in the same device. Further, as can be seen in Fig. 3b, the interleaved sequence fidelity is above the reference sequence in IRB measurement (note also some fidelities of above 100%). Although

IRB is easy to implement and analyse, and provides a mean for quick characterisation, it has its limitations. This is evidenced by the way that the interleaved gates can lead to extra decoupling from noise, as for example for the interleaved DCZ gate, which can make the interleaved sequences appear to have higher fidelities than the reference sequence especially for the lower amount of gate sequences.

To further understand both the time variation and the extra decoupling effects from interleaved gates, we examine the behaviour of the fidelity as a function of lab time using FBT. We divide the whole IRB run into several shorter sections, to which we apply the FBT analysis (see Supplementary Discussion: Implementation of Fast Bayesian Tomography for details). This allows us to plot the fidelity as a function of lab time, as shown in Fig. 3c. We believe that this drift in the fidelity is real and not an artefact of the tomographical analysis converging. The fidelity drifts, even in the of feedback, indicate that either our feedback is not good enough or the drift is affecting a component that is not part of the feedback.

In the Extended Table II one thing that becomes clear is that the single qubit fidelities are lower than the two qubit gate fidelities especially in devices B and C. In fact for our two qubit processor this is actually the limit of the overall operational fidelity. The breakdown of the errors extracted from the GST analysis in Extended Figs. 3 and 4 and the Extended Tables III(a) and III(b) reveals important aspects why this is the case. Firstly, we note from the Extended Tables III(a) and III(b) that on-target fidelity is much higher than the fidelity itself. What this means is that our control fidelity is high (even above 99.9% in device B), but because when we operate one qubit, the spectator qubits phase is decohering which

can be seen as IZ and ZI stochastic errors in Extended Fig. 3b, which means they are losing the phase information. In Device A in Extended Fig. 3a the Hamiltonian errors are larger in all physical gates though stochastic IZ and ZI error are still present. Further comparing the CZ results to DCZ we can see that both IZ and ZI in both Hamiltonian and stochastic errors are significantly suppressed. The pulse sequence for the DCZ cancels out the deterministic phase errors coming from the Stark shift and the decouples quasistatic single qubit noise suppressing also the stochastic phase errors.

In several experiments, we observed that the gates became less well calibrated for longer gate sequences. A reason for this are contextual errors that are caused by the shift of the Larmor frequency as a function of applied driving microwave power – an effect already observed earlier in silicon qubits [31–33]. We measure this Larmor shift for device A in Figure 4a, where we see especially strong dependency in qubit 1. This demonstrates a type of contextual error, where the same gate implementation is a slightly different operation at a different part of the sequence.

We further quantify this transient Larmor frequency shifts in Fig. 4b. To test how our gates are affected by this contextuality in device A, we initialise the two qubits in the $|\downarrow\downarrow\rangle$ state, execute a fixed number L of random gates from our selection of five different primitive gates and measure parity. We run 5000 different randomisation for each $L = 8, 16, 32, 64, 128$ with 100 single shots for each sequence. We use FBT to extract the process matrix for each L individually. As a consequence of this contextuality some components of the physical gates ($X_1^{\pi/2}$, $X_2^{\pi/2}$, and CZ) show a visible trend in Fig. 4b. Contextual errors can be measured and countered in principle, though for scalable operation an approach with more resilient gate implementation would be beneficial.

Discussion and Conclusions

The feasibility of consistently achieving fault-tolerant 2Q gate fidelities is essential for large-scale quantum computing. To simulate the conditions in a large array, we tested three different SiMOS devices, A, B, and C, through numerous experiments to determine the current variability and stability over time. Our 2Q gate implementations use pulsed interstitial exchange gates with a control range of 17 to 48 decades per volt. Our quantum characterisation, verification, and validation (QCVV) tools (IRB, FBT, and GST) offer a trade-off between quick, light analysis and computationally heavy, thorough analysis. Our peak fidelities are above the fault-tolerant threshold, but the variability in the gate fidelities (96.8% to 99.76%) is too high. Though some of the variation is caused by the different error characterisation methods, IRB, FBT and GST do estimate the error in a

differently. Possibly this leads to discrepancies between the fidelity numbers they yield.

Solving the limiting factors, such as excessive feedback and cross-talk, particularly in multi-qubit operations, could raise the average fidelity and lower variability. In two devices, A and B, feedback was necessary for both single and two qubits. In device C, feedback was not required, implying that further isotopic purification and stack development (such as improved oxide quality) may eliminate the need for feedback in a large array. Additionally, we identified an additional non-Markovian noise, Larmor frequency shift, which appears as contextual noise that requires further research to understand and mitigate.

For single qubit gates and CZ gates, the dominant source of error was T_2 -like decay for non-driven gates, reducing the fidelity from single qubit gates. However, using composite DCZ pulses reduced this error in the context of 2Q gates, with calibration error becoming the dominant source of error, suggesting potential for further improvement. In multi-qubit operations, single qubit operations are degraded due to $1/f$ noise on the idling qubit. This can be addressed using globally driven schemes that continuously decouple low frequencies ideally with increased Rabi frequencies [4, 22–25].

METHODS

Experimental devices

Three devices studied in this work were fabricated using multi-level aluminium gate-stack silicon MOS technology [34, 35] on isotopically enriched silicon-28 substrates of 800 ppm residual ^{29}Si (Device A & B) and of 50 ppm residual ^{29}Si (Device C). A layer of SiO_2 of ~ 8 nm was thermally grown above the silicon substrates. The devices are designed with plunger gate width of 30 nm and gate pitch as small as 50 nm. This allows a 20 nm gap between the plunger gates for J-gate to sit in the trenches.

Measurement Setup

Devices A is measured in an Oxford Kelvinox 400HA dilution refrigerator. DC bias voltages are coming from Stanford Research Systems SIM928 Isolated Voltage Sources. Gate pulse waveforms are generated with a Quantum Machines (QM) OPX+ and combined with DC biases using custom linear bias combiners at room temperature.

Devices B & C are measured in a Bluefors XLD400 dilution refrigerator. DC bias voltages are generated with Basel Precision Instruments SP927 DACs. Gate pulse waveforms are generated with a Quantum Machines OPX

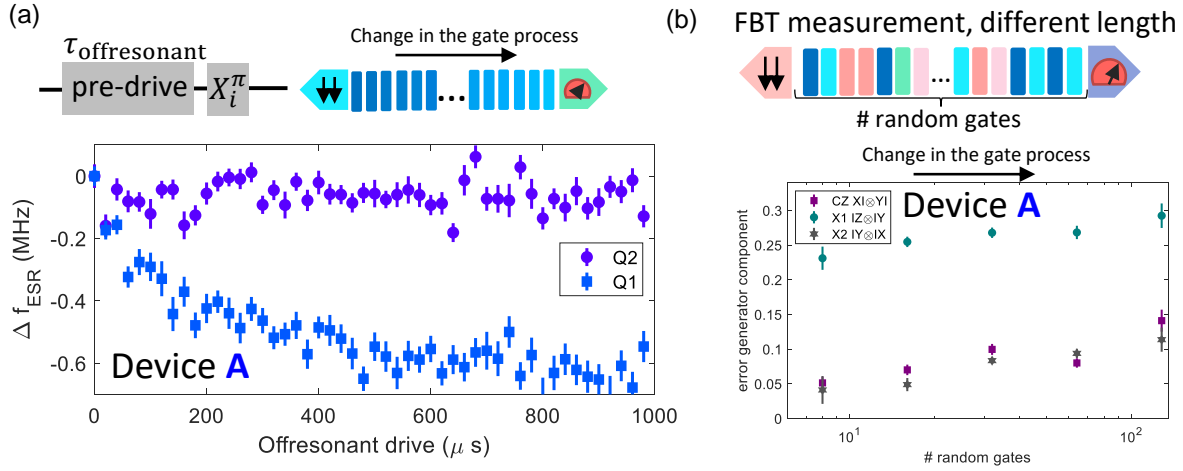


Figure 4 | Contextual errors. **a**, The Larmor frequency of both qubits in device A after applying an offresonant pre-pulse. The Q1 frequency shifts to lower frequencies with longer applied pre-pulse, due to a transient effect, possibly due to transient effects similar to Refs. [31–33]. This leads to contextual errors. **b**, Estimated gate noise channel components $\langle\langle XI||\Lambda_{CZ}||YI\rangle\rangle$, $\langle\langle IZ||\Lambda_{X1}||IY\rangle\rangle$ and $\langle\langle IY||\Lambda_{X2}||IX\rangle\rangle$ as a function of number of gates in a sequence. The shift indicates the changes in the process over the time of one shot of experiment.

and combined with DC biases using custom linear bias combiners at the 4 K stage.

The SET current of device A is amplified using a room temperature I/V converter (Basel SP983c) and sampled by a QM OPX. The SET of devices B & C are connected to a tank circuit with reflectometry measurement, with the tone generated by the QM OPX. The return signal is amplified by a Cosmic Microwave Technology CITFL1 LNA at the 4 K stage, and a Mini-circuits ZX60-P33ULN+ and Mini-circuits ZFL-1000LN+ at room temperature, before being digitised and demodulated with the QM OPXs.

For all devices, microwave pulses are generated with a Keysight PSG8267D Vector Signal Generator, with I/Q and pulse modulation waveforms generated from the QM OPXs.

DATA AVAILABILITY

The datasets generated and/or analysed during this study are available from the corresponding authors on reasonable request.

CODE AVAILABILITY

The analysis codes that support the findings of the study are available from the corresponding authors on reasonable request.

ACKNOWLEDGEMENTS

We thank A. Dickie and S. Serrano for technical help, T. Evans for help with FBT, and H. Stemp with GST. We acknowledge support from the Australian Research Council (FL190100167 and CE170100012), the US Army Research Office (W911NF-17-1-0198), and the NSW Node of the Australian National Fabrication Facility. The views and conclusions contained in this document are those of the authors and should not be interpreted as representing the official policies, either expressed or implied, of the Army Research Office or the US Government. The US Government is authorized to reproduce and distribute reprints for Government purposes notwithstanding any copyright notation herein. J.Y.H., W.G., R.S., M.F., A.E.S, and J.D.C. acknowledge support from Sydney Quantum Academy. C.O. S.S. K.M.R. and R.B.-K acknowledge support by the U.S. DOE/SC/ASCR through the Quantum Testbed Pathfinder Program. Sandia is a multiprogram laboratory managed and operated by NTESS, LLC., a wholly owned subsidiary of Honeywell International, Inc., for the U.S. DOE's NNSA under Contract No. DE-NA-0003525.

AUTHOR INFORMATION

Author Contributions

W.H.L. and F.E.H. fabricated the devices, with A.S.D.'s supervision, on isotopically enriched ^{28}Si wafers supplied by K.M.I. (800 ppm), N.V.A., H.-J.P., and M.L.W.T. (50 ppm). T.T. and W.H.L. measured initial devices and developed the final J-gate design. T.T. W.H.L. J.Y.H., N.D.S. and W.H.L. did the experi-

ments, coding and initial analysis, with A.M., A.L., A.S., C.H.Y., and A.S.D.'s supervision. R.C.C.L and W.H. helped with the initial experimental designs and ideas. R.Y.S. did the FBT analysis with supervision from S.D.B. and A.S. M.F. together with C.O., S.S., K.M.R. and R.B.-K. did the GST analysis. A.E.S. and N.D.S. did the feedback analysis. J.D.C. simulated the device structure to guide the gate design with supervision from C.C.E. and A.S. T.T. wrote the manuscript, with the input from all authors.

Corresponding Authors

Correspondence to the first or last authors.

COMPETING INTERESTS

A.S.D. is CEO and a director of Diraq Pty Ltd. Other authors declare no competing interest.

* t.tanttu@unsw.edu.au
 † current address: Quantum Motion Technologies Ltd
 ‡ current address: ETH Zurich
 § a.dzurak@unsw.edu.au

[1] Veldhorst, M. *et al.* An addressable quantum dot qubit with fault-tolerant control-fidelity. *Nature Nanotechnology* **9**, 981–985 (2014).

[2] Muhonen, J. T. *et al.* Storing quantum information for 30 seconds in a nanoelectronic device. *Nature Nanotechnology* **9**, 986–991 (2014).

[3] Yoneda, J. *et al.* A quantum-dot spin qubit with coherence limited by charge noise and fidelity higher than 99.9%. *Nature Nanotechnology* **13**, 102–106 (2017).

[4] Yang, C. H. *et al.* Silicon qubit fidelities approaching incoherent noise limits via pulse engineering. *Nature Electronics* **2**, 151–158 (2019).

[5] Yang, C. H. *et al.* Operation of a silicon quantum processor unit cell above one kelvin. *Nature* **580**, 350–354 (2020).

[6] Petit, L. *et al.* Universal quantum logic in hot silicon qubits. *Nature* **580**, 355–359 (2020). URL <https://doi.org/10.1038/s41586-020-2170-7>.

[7] Fowler, A. G., Mariantoni, M., Martinis, J. M. & Cleland, A. N. Surface codes: Towards practical large-scale quantum computation. *Physical Review A* **86**, 032324 (2012).

[8] Mądzik, M. T. *et al.* Precision tomography of a three-qubit donor quantum processor in silicon. *Nature* **601**, 348–353 (2022).

[9] Noiri, A. *et al.* Fast universal quantum gate above the fault-tolerance threshold in silicon. *Nature* **601**, 338–342 (2022).

[10] Xue, X. *et al.* Quantum logic with spin qubits crossing the surface code threshold. *Nature* **601**, 343–347 (2022).

[11] Mills, A. R. *et al.* Two-qubit silicon quantum processor with operation fidelity exceeding 99%. Preprint at <https://arxiv.org/abs/2111.11937> (2021).

[12] Weinstein, A. J. *et al.* Universal logic with encoded spin qubits in silicon. *Nature* (2023). URL <https://doi.org/10.1038/s41586-023-05777-3>.

[13] Huang, W. *et al.* Fidelity benchmarks for two-qubit gates in silicon. *Nature* **569**, 532–536 (2019). URL <https://doi.org/10.1038/s41586-019-1197-0>.

[14] Philips, S. G. J. *et al.* Universal control of a six-qubit quantum processor in silicon. *Nature* **609**, 919–924 (2022). URL <https://doi.org/10.1038/s41586-022-05117-x>.

[15] Watson, T. F. *et al.* A programmable two-qubit quantum processor in silicon. *Nature* **555**, 633–637 (2018). URL <https://doi.org/10.1038/nature25766>.

[16] Knill, E. *et al.* Randomized benchmarking of quantum gates. *Phys. Rev. A* **77**, 012307 (2008). URL <https://link.aps.org/doi/10.1103/PhysRevA.77.012307>.

[17] Magesan, E. *et al.* Efficient measurement of quantum gate error by interleaved randomized benchmarking. *Phys. Rev. Lett.* **109**, 080505 (2012). URL <https://link.aps.org/doi/10.1103/PhysRevLett.109.080505>.

[18] Greenbaum, D. Introduction to quantum gate set tomography. *arXiv preprint arXiv:1509.02921* (2015).

[19] Nielsen, E. *et al.* Gate Set Tomography. *Quantum* **5**, 557 (2021).

[20] Evans, T. *et al.* Fast bayesian tomography of a two-qubit gate set in silicon. *Phys. Rev. Applied* **17**, 024068 (2022). URL <https://link.aps.org/doi/10.1103/PhysRevApplied.17.024068>.

[21] Bonilla Ataides, J. P., Tuckett, D. K., Bartlett, S. D., Flammia, S. T. & Brown, B. J. The xzzx surface code. *Nature Communications* **12**, 2172 (2021). URL <https://doi.org/10.1038/s41467-021-22274-1>.

[22] Vahapoglu, E. *et al.* Single-electron spin resonance in a nanoelectronic device using a global field. *Science Advances* **7**, eabg9158 (2021). URL <https://www.science.org/doi/abs/10.1126/sciadv.abg9158>. <https://www.science.org/doi/pdf/10.1126/sciadv.abg9158>.

[23] Hansen, I. *et al.* Pulse engineering of a global field for robust and universal quantum computation. *Phys. Rev. A* **104**, 062415 (2021). URL <https://link.aps.org/doi/10.1103/PhysRevA.104.062415>.

[24] Seedhouse, A. E. *et al.* Quantum computation protocol for dressed spins in a global field. *Phys. Rev. B* **104**, 235411 (2021). URL <https://link.aps.org/doi/10.1103/PhysRevB.104.235411>.

[25] Hansen, I. *et al.* Implementation of an advanced dressing protocol for global qubit control in silicon. *Applied Physics Reviews* **9**, 031409 (2022). URL <https://doi.org/10.1063/5.0096467>. <https://doi.org/10.1063/5.0096467>.

[26] Gilbert, W. *et al.* On-demand electrical control of spin qubits. *Nature Nanotechnology* (2023). URL <https://doi.org/10.1038/s41565-022-01280-4>.

[27] Johnson, A. C., Petta, J. R., Marcus, C. M., Hanson, M. P. & Gossard, A. C. Singlet-triplet spin blockade and charge sensing in a few-electron double quantum dot. *Phys. Rev. B* **72**, 165308 (2005). URL <https://link.aps.org/doi/10.1103/PhysRevB.72.165308>.

[28] Seedhouse, A. E. *et al.* Pauli blockade in silicon quantum dots with spin-orbit control. *PRX Quantum* **2**, 010303 (2021).

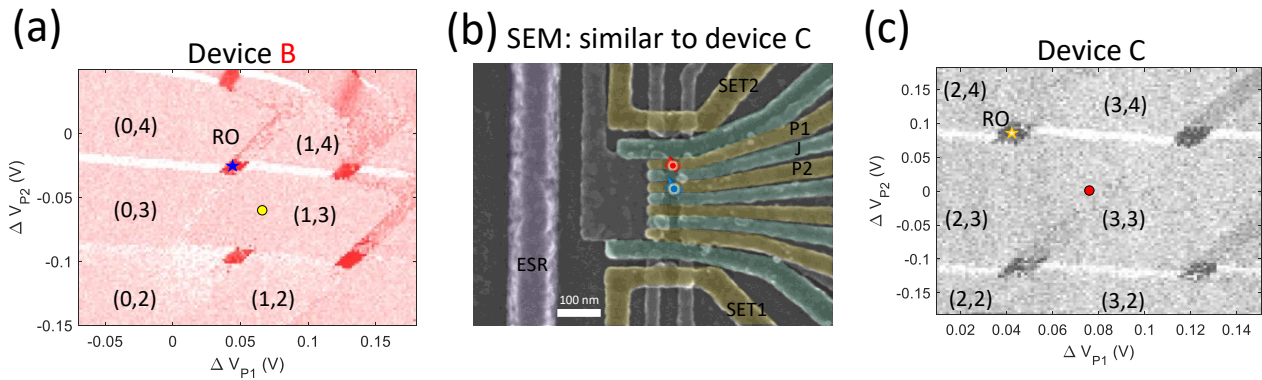
- [29] Nielsen, E. *et al.* Probing quantum processor performance with pygsti. *Quantum Science and Technology* **5**, 044002 (2020). URL <https://dx.doi.org/10.1088/2058-9565/ab8aa4>.
- [30] Blume-Kohout, R. *et al.* A taxonomy of small markovian errors. *PRX Quantum* **3**, 020335 (2022). URL <https://link.aps.org/doi/10.1103/PRXQuantum.3.020335>.
- [31] Freer, S. *et al.* A single-atom quantum memory in silicon. *Quantum Science and Technology* **2**, 015009 (2017). URL <https://dx.doi.org/10.1088/2058-9565/aa63a4>.
- [32] Takeda, K. *et al.* Optimized electrical control of a Si/SiGe spin qubit in the presence of an induced frequency shift. *npj Quantum Information* **4**, 54 (2018).
- [33] Undseth, B. *et al.* Nonlinear response and crosstalk of electrically driven silicon spin qubits (2022). URL <https://arxiv.org/abs/2205.04905>.
- [34] Angus, S. J., Ferguson, A. J., Dzurak, A. S. & Clark, R. G. A silicon radio-frequency single electron transistor. *Applied Physics Letters* **92**, 112103 (2008).
- [35] Lim, W. H. *et al.* Observation of the single-electron regime in a highly tunable silicon quantum dot. *Applied Physics Letters* **95**, 242102 (2009).

Extended Data Table I. Device table. Comparison table of the characteristics and operation principles of all the devices used in this experimental campaign.

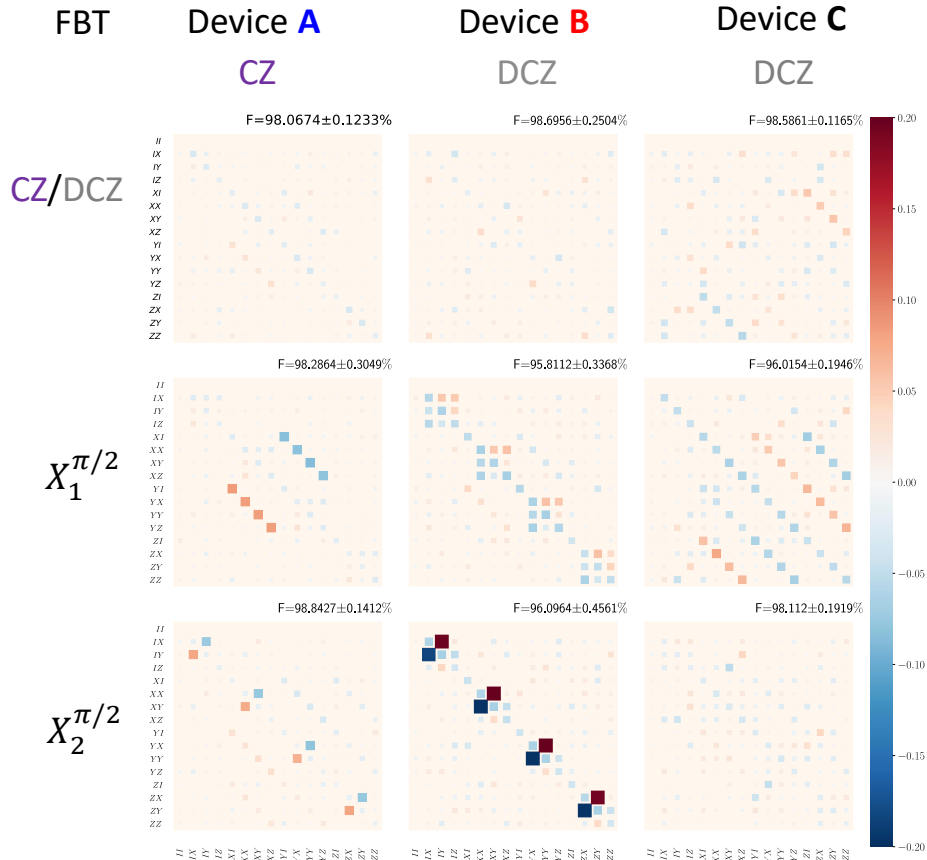
Device	Device A		Device B		Device C	
$T_2^*(\mu s)$ Q1,Q2	5.5 ± 0.3	6.5 ± 0.3	3.0 ± 0.3	2.6 ± 0.3	5.5 ± 0.3	5.5 ± 0.3
$T_2^{\text{Hahn}}(\mu s)$ Q1,Q2	51 ± 3	60 ± 3	39 ± 3	46 ± 3	132 ± 3	72 ± 3
$T_2^{\text{Rabi}}(\mu s)$ Q1,Q2	55 ± 5	64 ± 5	26 ± 3	56 ± 3	131 ± 5	100 ± 5
$X^{\pi/2}(\mu s)$ Q1,Q2	0.520	0.400	0.200	0.380	0.326	0.200
1Q RB fidelity	99.5%	99.6%	99.6%	99.7%	-	-
ΔE_Z (MHz)	10.8		22.7		12.95	
J-gate turn on (dec/V)	17.13		45.15		20.64	
Initialisation	T^- (Heralded)		$\uparrow\downarrow$		T^- (Heralded)	
B_0 and orientation	0.8274 T, [100]		0.893 T, [110]		0.790 T, [110]	
Charge configuration	(1,3) Isolated		(1,3) Reservoir		(3,3) Reservoir	
Parity readout visibility	98 %		99 %		95 %	
GST gauge <i>invariant</i> SPAM fidelity	97.6 ± 0.9 %		98.4 ± 0.4 %		-	
Single shot time (μs)	1000		100		200	
Residual ^{29}Si	800 ppm		800 ppm		50 ppm	
Design # dots	three		three		four	
Feedbacks	$I_{\text{SET}}, \epsilon, f_{\text{ESR}}, P_{X_i}^{\text{Q1}}, V_{\text{CZ}}, \varphi_{\text{CZ}}^{\text{Q1}}$		$I_{\text{SET}}, \epsilon, f_{\text{ESR}}, P_{X_i}^{\text{Q1}}, V_{\text{DCZ}}$		I_{SET}	

Extended Data Table II. Fidelities extracted from several experimental error characterisation runs. FBT results are from one of the IRB runs indicated by italics. Mean and standard deviation (std) of all IRB runs for for a given device. The error bars for IRB come from the error bars of the fit and for FBT we report the average fidelity over the experiment with error bars being the 2σ variation over the experiment. For GST the error bars given by the error of the log-likelihood fit. Some of these are also plotted in the main text figure 3

Run/Gate	Clifford (%)	CZ/DCZ(%)	$X_1^{\pi/2}$ (%)	$X_2^{\pi/2}$ (%)
IRB ₁ A	90.78 ± 0.10	98.43 ± 0.22	-	-
IRB ₂ A	90.71 ± 0.06	98.41 ± 0.13	-	-
mean,std A	90.75 ± 0.05	98.42 ± 0.01	-	-
IRB ₃ B	86.95 ± 0.19	99.00 ± 0.28	-	-
IRB ₄ B	89.65 ± 0.06	99.39 ± 0.11	-	-
IRB ₅ B	85.06 ± 0.10	99.33 ± 0.20	-	-
IRB ₆ B	84.93 ± 0.09	100.01 ± 0.17	-	-
IRB ₇ B	86.13 ± 0.07	99.32 ± 0.14	-	-
IRB ₈ B	87.52 ± 0.07	99.28 ± 0.14	-	-
IRB ₉ B	87.29 ± 0.08	99.20 ± 0.15	-	-
IRB ₁₀ B	86.90 ± 0.11	99.68 ± 0.26	-	-
IRB ₁₁ B	87.19 ± 0.07	99.14 ± 0.12	-	-
mean,std B	86.85 ± 1.41	99.37 ± 0.3	-	-
IRB ₁₂ C	89.69 ± 0.11	99.81 ± 0.29	-	-
IRB ₁₃ C	88.02 ± 0.13	99.51 ± 0.28	-	-
IRB ₁₄ C	90.52 ± 0.09	99.70 ± 0.23	-	-
IRB ₁₅ C	89.08 ± 0.10	100.02 ± 0.24	-	-
mean,std C	89.33 ± 1.05	99.76 ± 0.20	-	-
FBT A	-	98.35 ± 0.54	98.41 ± 0.89	99.09 ± 0.78
FBT B	-	99.03 ± 0.91	95.92 ± 0.78	96.58 ± 0.66
FBT C	-	99.04 ± 0.54	97.00 ± 1.16	97.72 ± 0.87
GST A	-	96.8 ± 0.2	96.5 ± 0.2	97.5 ± 0.2
GST B	-	98.0 ± 0.1	97.9 ± 0.2	95.7 ± 0.2



Extended Data Fig. 1 | Devices B and C stability maps and SEM of a device similar to C **a**, Device B stability map. Operation point (OP) and readout point (RO) indicated together with the charge occupancy states in **b**, Scanning electron micrograph (SEM) of device similar to C. **c**, Device C stability map. Indication same as in a



Extended Data Fig. 2 | Error generators from FBT analysis, Devices A, B and C, for single and two qubit gates.

FBT estimated gate error generators for each device are analysed from IRB experiments individually. Plotted error generators are the posterior of the last update of each analysis. Fidelity and its uncertainty (with 95% confidence interval) are calculated by re-sampling with the Gaussian statistic of the final estimated results.

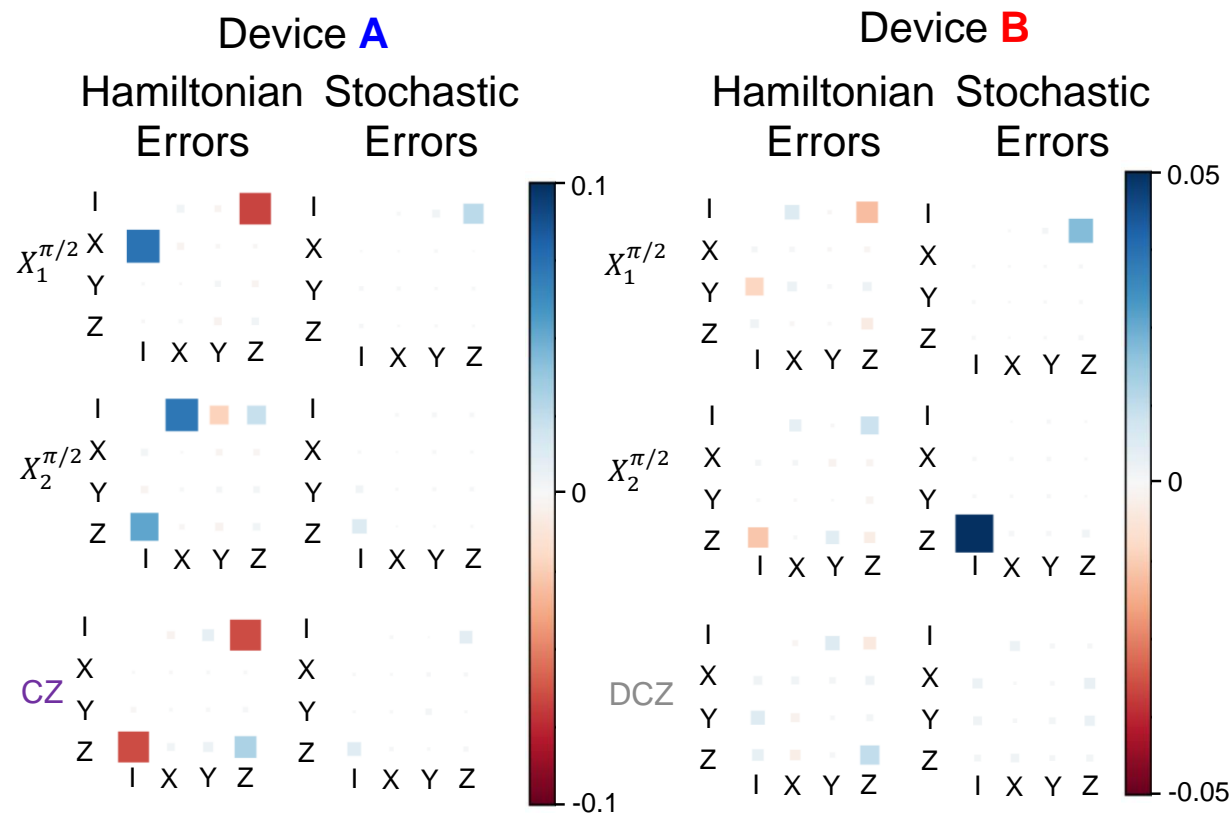
Extended Data Table III. Error metrics from GST characterization of (a) device A and (b) device B, partitioned by qubit support. Generator infidelities and total error are defined in equations 4 and 5 of the supplementary material. For both metrics we have broken down the total infidelity/error into their contributions from each of the qubits. The on-target generator fidelity corresponds to the fidelity with which a given gate enacts the ideal gate operation on the qubit being targeted. By breaking down the infidelity based on the support of the operations we can see that a significant contribution to the single qubit gate error budget comes from crosstalk errors inducing undesired evolution on the spectator qubit.

Gate	On-Target Generator Fidelity	Generator Infidelity			Total Error		
		On Q1	On Q2	Total	On Q1	On Q2	Total
$X_1^{\pi/2}$	99.3(4)%	0.7(4)%	3.5(4)%	4.5(8)%	7.6(5)%	9.8(6)%	13.6(8)%
$Z_1^{\pi/2}$	99.9(3)%	0.1(3)%	0.2(3)%	0.3(6)%	0.3(4)%	2.5(4)%	2.8(7)%
$X_2^{\pi/2}$	99.1(4)%	2.0(4)%	0.9(4)%	3.3(7)%	7.0(5)%	8.2(4)%	11.9(7)%
$Z_2^{\pi/2}$	99.9(3)%	0.2(3)%	0.1(3)%	0.4(6)%	1.1(6)%	2.6(4)%	3.1(6)%
CZ	95.9(7)%	1.7(4)%	1.5(4)%	4.1(8)%	7.8(4)%	7.7(4)%	12.9(8)%

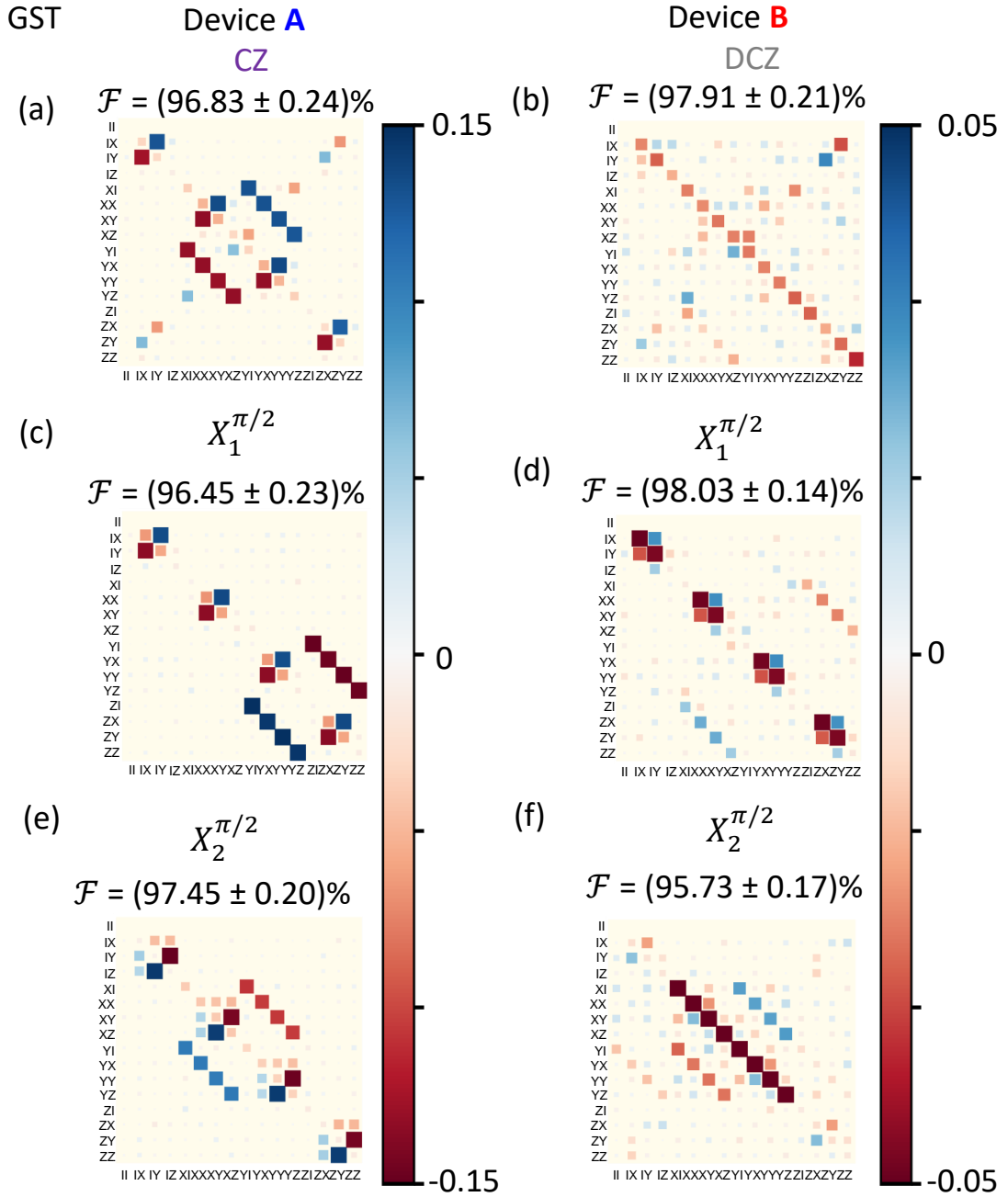
(a) Device A

Gate	On-Target Generator Fidelity	Generator Infidelity			Total Error		
		On Q1	On Q2	Total	On Q1	On Q2	Total
$X_1^{\pi/2}$	99.9(3)%	0.1(3)%	2.3(3)%	2.7(6)%	1.2(5)%	4.0(4)%	4.7(6)%
$Z_1^{\pi/2}$	99.9(6)%	0.1(3)%	0.2(3)%	0.4(6)%	0.5(4)%	1.1(4)%	1.4(7)%
$X_2^{\pi/2}$	99.9(2)%	5.1(3)%	0.1(2)%	5.6(4)%	6.4(4)%	1.2(4)%	7.5(5)%
$Z_2^{\pi/2}$	99.9(2)%	0.1(2)%	0.1(2)%	0.4(5)%	0.4(3)%	1.1(3)%	1.5(5)%
DCZ	97.5(5)%	0.7(2)%	0.4(2)%	2.5(5)%	1.4(3)%	1.3(3)%	4.2(6)%

(b) Device B



Extended Data Fig. 3 | Hamiltonian and Stochastic Error Generators from GST reports for devices A and B
a, Color bar ranges from -0.1 to +0.1 **b**, Color bar ranges from -0.05 to +0.05



Extended Data Fig. 4 | Gate Set Tomography, Devices A and B

a, Full error generator for device A, CZ gate. **b**, Full error generator for device B, DCZ gate. **c**, Full error generator for device A, $X_1^{\pi/2}$. **d**, Full error generator for device B, $X_1^{\pi/2}$. **e**, Full error generator for device A, $X_2^{\pi/2}$. **f**, Full error generator for device B, $X_2^{\pi/2}$.